Water Research, Volume 203, September 2021, Article number 117531
DOI:10.1016/j.watres.2021.117531

Bactericidal efficiency and photochemical mechanisms of micro/nano bubble–enhanced visible light photocatalytic water disinfection

Wei Fan [a], Jingyu Cui [a], Qi Li [a], Yang Huo [b], Dan Xiao [c], Xia Yang [a], Hongbin Yu [a], Chunliang Wang [b,*], Peter Jarvis [d], Tao Lyu [d,*], Mingxin Huo [a]

[a] *School of Environment, Northeast Normal University, 2555 Jingyue Street, Changchun, 130117, China*

[b] *National Demonstration Center for Experimental Physics Education, Northeast Normal University, Changchun 130024, China*

[c] *Jilin Academy of Agricultural Science, 1363 Shengtai Street, Changchun, 130033, China*

[d] *Cranfield Water Science Institute, Cranfield University, College Road, Cranfield, Bedfordshire, MK43 0AL, UK*

Corresponding authors: wangclnenu@163.com (C.W.). t.lyu@cranfield.ac.uk (T.L.)

Abstract

Microbial contamination of water in the form of highly-resistant bacterial spores can cause a long-term risk of waterborne disease. Advanced photocatalysis has become an effective approach to inactivate bacterial spores due to its potential for efficient solar energy conversion alongside reduced formation of disinfection by-products. However, the overall efficiency of the process still requires significant improvements. Here, we proposed and evaluated a novel visible light photocatalytic water disinfection technology by its close coupling with micro/nano bubbles (MNBs). The inactivation rate constant of *Bacillus subtilis* spores reached 1.28 h^{-1}, which was 5.6 times higher than that observed for treatment without MNBs. The superior performance for the progressive destruction of spores' cells during the treatment was confirmed by transmission electron microscopy (TEM) and excitation-emission matrix (EEM) spectra determination. Experiments using scavengers of reactive oxygen species (ROSs) revealed that H_2O_2 and $\cdot OH$ were the primary active species responsible for the inactivation of spores. The effective supply of oxygen from air MNBs helped accelerate the hole oxidation of H_2O_2 on the photocatalyst (i.e. Ag/TiO_2). In addition, the interfacial photoelectric effect from the MNBs was also confirmed to contribute to the spore inactivation. Specifically, MNBs induced strong light scattering, consequently increasing the optical path length in the photocatalysis medium by 54.8% at 700nm and enhancing light adsorption of the photocatalyst. The non-uniformities in dielectricity led to a high-degree of heterogeneity of the electric field, which triggered the formation of a region of enhanced light intensity which ultimately promoted the photocatalytic reaction. Overall, this study provided new insights on the mechanisms of photocatalysis coupled with MNB technology for advanced water treatment.

Keywords: Light scattering; microbial spores; nanobubble technology; photodegradation; reactive oxygen species

1. Introduction

Waterborne diseases are transmitted through microorganisms such as viruses, bacteria and protozoa (Dalrymple et al., 2010). Among such microbial contaminants, bacteria spores are the most dormant form of bacteria and can survive for many decades. They are extremely resistant to environmental stresses including high ambient temperature, pressure and radiation, and can co-exist with toxic chemicals (Setlow, 2014). The resistance is mainly attributed to 1) the dehydrated, highly mineralised core enclosed in a thick protective spore coat, and 2) the saturation of their DNA with small, acid-soluble spore proteins that greatly alters the enzymatic reactivity of the DNA (Leggett et al., 2012; Setlow, 2014; Sella et al., 2014). Once the spore is exposed to more favourable conditions, it can resume the growth process and potentially spread waterborne diseases (Li et al., 2018). Therefore, technology development for the destruction and inactivation of bacteria spores has attracted great attention in the field of water disinfection.

Commonly used disinfection processes such as ozonation, chlorination and germicidal ultraviolet radiation have been used and investigated for inactivation of bacterial spores (Setlow et al., 2002). Research has shown that chlorination treatment using chlorine dioxide (ClO_2) can eliminate hydrogen peroxide resistant *Bacillus pumilus* SAFR-032 spores, from

$1.3x10^5$ µg/mL to undetectable levels after 24 hours (Friedline et al., 2015). Chlorine-resistant *Bacillus cereus* spores were inactivated by ozonation (O_3) treatment (Ding et al., 2019). However, these oxidants (ClO_2 and O_3) can interact with components in the background water matrix (dissolved organic matter, intracellular organic matter, algal matter) leading to the formation of unwanted disinfection by-products (or their precursors), which have been linked with possible adverse health effects (Ding et al., 2019; Zhong et al., 2019). Ultraviolet (UV) irradiation is another process that has been used for the disinfection of spores such as *Bacillus subtilis* strain MW01 (Wassmann et al., 2012). However, all of these processes require expensive chemicals and/or costly equipment to generate the disinfectant on-site.

Addressing this issue requires novel ways of treating the spores using processes that have lower cost, less energy consumption and reduced secondary environmental impacts. Photocatalysis is becoming a viable option because of its potential to use sunlight to drive the disinfection process using a solid catalyst such as titanium dioxide (TiO_2) (Xia et al., 2015; McGivney et al., 2017; Zhou et al., 2020). The relatively high disinfection capacity is attributed to the production of photon-excited reactive oxygen species (ROSs), including electrons (e^-), holes (h^+), $\cdot OH$, H_2O_2 and $\cdot O_2^-$. Previous studies have shown that H_2O_2 can penetrate approximately 4 µm into the spore's cell wall within 1 ms (Lim et al., 2016), enabling the synergetic bactericidal processes to be triggered by all ROSs. However, the e^- and h^+ can easily recombine in the solution, and the half-lives of $\cdot OH$ and $\cdot O_2^-$ are only approximately 10^{-9} and 10^{-6} s, respectively (Phaniendra et al., 2015). Such drawbacks reduce the capacity of ROSs in being able to penetrate the coat and cell membrane of the spore, preventing attack of the intracellular DNA (Du et al., 2016).

In order to suppress e^-/h^+ recombination and enhance the generation of ROSs, efforts including surface modification and nanocrystallization of the photocatalyst (Jiang et al., 2017; Parangi and Mishra, 2019; Hu et al., 2020), and design/optimization of novel reactors (Athanasiou et al., 2016) have been made in photocatalysis processes. However, these methods require complicated manufacturing and a high associated cost. In this study, we proposed a novel alternative mico/nano bubble (MNB) approach to enhance aqueous disinfection of spores using visible light photocatalysis. MNBs are ultrafine gas-filled bubbles in the micro/nanometer size range. These bubbles possess several important characteristics, including low buoyancy, slow rising velocity, and a high internal gas density state (Fan et al., 2020; John et al., 2020; Wang et al., 2021a). Due to the larger relative surface area and their longevity, MNBs containing air can sustainably supply oxygen to the surrounding water (Zhang et al., 2006; Lyu, et al., 2019). This feature is proposed to assist in removing the excited electrons, preventing recombination of the electron-hole pair (Almquist and Biswas, 2001). Moreover, small bubbles have high single-scattering albedo in the solution (Churnside, 2010). As such, the electromagnetic illumination could drive the electric charges near the bubble into oscillatory motion and lead to secondary radiation (Bohren and Huffman, 2008). The smaller the bubble is, the longer the wavelength will be. As a consequence, stronger lateral/backward scattering intensity might be achieved from MNBs (Bohren and Huffman, 2008; Kim and Chang, 2017). Therefore, it was hypothesised that this light scattering effect could improve the light efficiency in photocatalytic reactions. To the best of our knowledge, the effect of MNBs on photocatalytic disinfection and the underpinning mechanisms have not been studied previously.

The present study assessed the bactericidal effectiveness and unveiled the photochemical mechanisms of the proposed MNB process coupled with visible light photocatalytic disinfection. The *Bacillus subtilis* spore was chosen as the model microbial contaminant as it is one of the most commonly found spore forming bacteria in water. The bactericidal efficiency was investigated through monitoring the inactivation rate and the progressive destruction of spores by transmission electron microscopy (TEM) and excitation-emission matrix (EEM) spectra analysis. An ROS scavenging experiment was carried out to identify the main reactive radicals that contribute to the spore inactivation. Moreover, the influences of MNBs on O_2 supply and light scattering during photocatalysis was also determined. The photochemical mechanisms during the process were confirmed by Mie theory computational and finite difference time domain (FDTD) model simulations.

2. Materials and methods

2.1. Preparation and characterisation of photocatalyst and micro/nano bubbles

Nanosized Ag/TiO_2 particles were prepared as the photocatalyst through a sol-gel process (Lee et al. 2005). The topography and particle size of the photocatalyst were observed using high-resolution transmission electron microscopy (HRTEM) and the elements were detected using energy dispersive x-ray spectroscopy (EDS) (SEI Model XL30-ESEM, Philips, Netherland). The major phase of the synthesised particles was analysed by an X-ray diffractometer (XRD) (Dmax 2200 PC, Rigaku, Japan) using Cu Kα radiation. The UV-vis diffuse reflection spectra was acquired by a UV-vis-NIR Varian Cary 500 spectrophotometer. X-ray photoelectron spectroscopy (XPS, Thermo Scientific Kα, USA) were used to obtain the high resolution XPS spectra of C1s, O1s, Ti 2p, and Ag 3d in Ag/TiO_2.

MNB emulsion was prepared in the sterilized distilled water using an MNB generator (Model XZCP-K-0.75, Xiazhichun, China) following the cavitation concept. The generator was operated for 25 min before using for subsequent photocatalytic experiments. The number and size distribution of MNBs were determined by a Multisizer 4e counter (Beckman Coulter, Brea, USA). The characteristic size of the MNBs was described by the Sauter mean diameter (Wang et al., 2018), and the DO was monitored by a PreSens DO probe (Fibox 4, Germany). In order to obtain an equivalent DO condition in the control treatment group, conventional aeration was conducted by an air blower and a porous plate diffuser (Songbao SB718, China), resulting in millimetre-sized bubbles (Fan et al., 2020). Pre-aerated water was then introduced into the photocatalytic reactor (section 2.3).

2.2. Bacterial and Sporulation

Bacillus subtilis strain CMCC63501 was used as an indicator microorganism in this study. Cells of the strain were grown in Luria-Bertani (LB) medium at 37 ºC to their mid-exponential growth phase. Colonies of *Bacillus subtilis* were transferred and incubated in 1/10 nutrition for 7 days to form spores following the procedures described by Choi et al. (2007) and Jung et al. (2008). The spores were washed from the medium using DI water and centrifuged three times (Li et al., 2018). The remaining spore suspension was heated to 80 ºC and then held at that temperature for 10 min using a thermostatically controlled water bath to inactivate any remaining *Bacillus subtilis* cells. The numbers of spores were measured through diluted plate counting, and the initial concentration of spores in the following experiments was approximately 10^5 CFU/mL.

2.3. Photocatalytic unit setup and experimental operation

The photocatalytic disinfection experiments were performed in 2.75×9.5 cm (diameter×height) glass reactors. The visible light irradiation was performed on the side using a 300 W-xenon lamp (100 mW/cm^2, CERMAX-LX-300, USA) through a 420 nm cut-off filter (HOYA Glass Co., Japan). 40 mL of the homogenised spore solution (10^5 CFU/mL) was added to the reactor. The concentration of the photocatalyst (Ag/TiO_2) was 1 g/L. The survival ratios of spores by the application of MNB-aerated water as the solution (MNBs group) was compared with the control group without the application of MNBs. An experiment with catalyst and MNB but no irradiation was also conducted to obtain the bactericidal baseline.

After preparation, all systems were monitored for 1 hour and the sampling interval was 10 min. The samples were used to determine the survival ratio of the spores, where the colonies of germinated spores were identified and counted after 12 h incubation at 37 ^oC by a spread plate technique. Inactivation rates (k) of spores were calculated from the slopes of the $-\ln(C_t/C_0)$ / t regressive lines, where C_t denoted the spore concentration at time t, and C_0 was the initial spore concentration. The morphology and structural changes of spores during the photocatalytic processes were determined at the beginning and end of the experiment. EEM analysis was employed to evaluate the fluorescence properties and the structure of the released intracellular substances of spore at excitation wavelengths from 220-450 nm and emission wavelengths from 280-510 nm at 5 nm intervals (LS-55, PerkinElmer, USA). The morphology of spores was investigated by TEM (Du et al. 2016). All materials used in the experiments were pre-sterilised, and all experimental groups were conducted in duplicate and sample analysis was conducted in triplicate.

2.4. Investigation of the MNBs induced bactericidal mechanisms

2.4.1. ROSs scavenging experiment

To identify the specific role of individual ROS in the proposed bactericidal process, an ROS scavenging experiment was conducted under the same experimental conditions as described in Section 2.3. Four radical scavengers, i.e. sodium oxalate (0.5 mmol/L), isopropanol (0.5 mmol/L), Fe (II)-EDTA (0.1 mmol/L), and TEMPOL (2 mmol/L), were added in the initial solutions to quench h^+, ·OH, H_2O_2, and $\cdot O_2^-$, respectively (Du et al., 2016). The samples from the MNB treatment and control groups were collected to monitor the survival rates of the bacterial spores.

2.4.2. The effect of the O_2 supply from MNBs

Increased O_2 supply from air MNBs could come from two possible routes. Firstly, the superaturation of O_2 from the hydrodynamic cavitation during the MNB generation. Secondly, from the sustainable diffusion of O_2 from MNBs due to their longevity and high specific surface area. To investigate, the experiment in Section 2.3 was repeated for a system with and without MNBs present. An additional experiment was carried out using nitrogen filled MNBs to slightly degas the above-mentioned air MNBs solution (where the DO was over 10 mg/L) until the initial DO reached 8.80 mg/L to enable a comparison to be made with the control group experiments of similar initial DO. During the experimental period, the survival rates of the bacterial spores and the DO concentrations were determined with an oxygen micro-sensor (Fibox 4, Germany).

2.4.3. Modelling of MNBs-induced light scattering

Following classical electromagnetic theory, light scattering of an MNB triggered by charge excitation or re-radiation of the electromagnetic energy can be schematically illustrated (Fig. 1). The scattering is identical at all polar angles φ, while the distribution of the scattered intensities at different angles θ has a great influence on light propagation. Therefore, in this study, Mie theory was applied to calculate the scattering properties, which provided an analytical solution of Maxwell's equations for the scattering of electromagnetic radiation by spherical particles in terms of infinite series (Wriedt, 2012). The scattering spectra of a single MNB or spore (the scattering phase function) and the relative scattering intensity at specific propagation distance were calculated using the Mie computational package: PyMieScatt

(Sumlin et al., 2018). Calculation details are shown in the Supporting Information (SI, Text S1). The finite difference time domain (FDTD) model was applied to numerically simulate the ne ar field optical properties (SI, Text S2). A plane-wave and the polarization were set to be the x and y-axis, respectively (Fig. 1). A field and power monitor in the frequency domain was used to record the electrical intensity ($|E|^2$ representing the optical intensity). Three scenarios of FDTD modelling were simulated: 1) water alone; 2) single MNB, single spore, and single Ag/TiO_2 particle; and 3) 50 Ag/TiO_2 particles placed at the surface of the spore with an MNB placed closely to the spore.

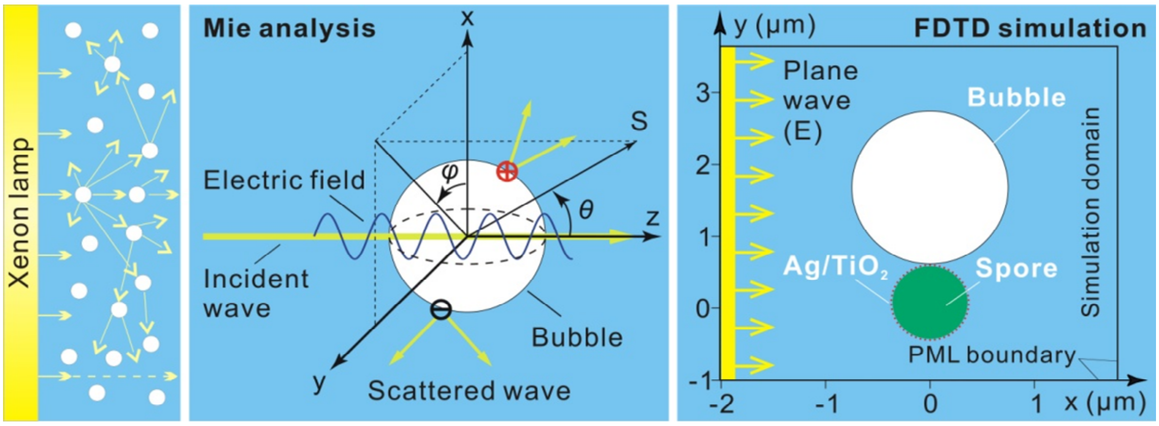

Fig. 1. Schematic of light scattering induced by bubble and the 2D FDTD model formulation.

3. Results and discussion

3.1. Characterisation of the photocatalyst and MNBs

The prepared Ag/TiO_2 photocatalyst had an average particle diameter of 22.8 nm and contained 0.76% (w/w) of Ag in the doped TiO_2 (Fig. 2a). The high resolution XPS spectra of C1s, O1s, Ti 2p, and Ag 3d in Ag/TiO_2 indicated that the main crystal type of TiO_2 was confirmed to be the anatase phase (2θ=25.3, 37.4, 47.3, and 54.3°) (Xin et al., 2020) (Fig. S1). The bandgap energy (E_g) for the photocatalyst was determined by a Tauc plot, $(Ah\upsilon)^{0.5} = A(h\upsilon\text{-}E_g)$ (Fig. 2b) (Chen et al., 2019). The values of E_g for Ag/TiO_2 and TiO_2 were 1.5 and 3.1 eV, respectively, showing a substantial band gap reduction and a distinct redshift after Ag-doping. Considering that bandgap narrowing may lead to more absorption of visible light and photogenerated electron transfer (Xing et al., 2014), the prepared Ag/TiO_2 was considered suitable for enhancement of the photocatalytic disinfection performance under visible light irradiation.

The total number of MNBs in the suspension was 1.84×10^5 particles/mL with a Sauter mean diameter of 2.7 µm (Fig. 2c). Approximately 30% of the bubbles present were in the nanometer range (<1 µm). There was a significantly higher DO (10.49 mg/L) in the MNB-aerated water compared to the water aerated using macro-bubbles (8.89 mg/L) after 20 mins of operation (Fig. 2d). Previous studies have reported that MNB application can induce a gas supersaturated condition (Wu et al., 2019) which was consistent with the observations seen here. The ultrafine bubbles have a greater surface area per unit volume and can therefore increase the O_2 gas transfer rate into the surrounding water (Fan et al., 2021a). In turn, this is expected to enable more efficient activation of the electron hole during photodegradation (Almquist and Biswas, 2001). More importantly, Zhang et al., (2006) confirmed the high-gas-density state in nanobubbles, where the inner gas may exist as an aggregation, rather than an ideal gas phase, and the diffusion of the inner gas is likely to be slow and take place over a long period. Thus, the ultrafine bubbles may act as an 'O_2 bank' to sustainably supply O_2 during the process and promote the photocatalytic treatment.

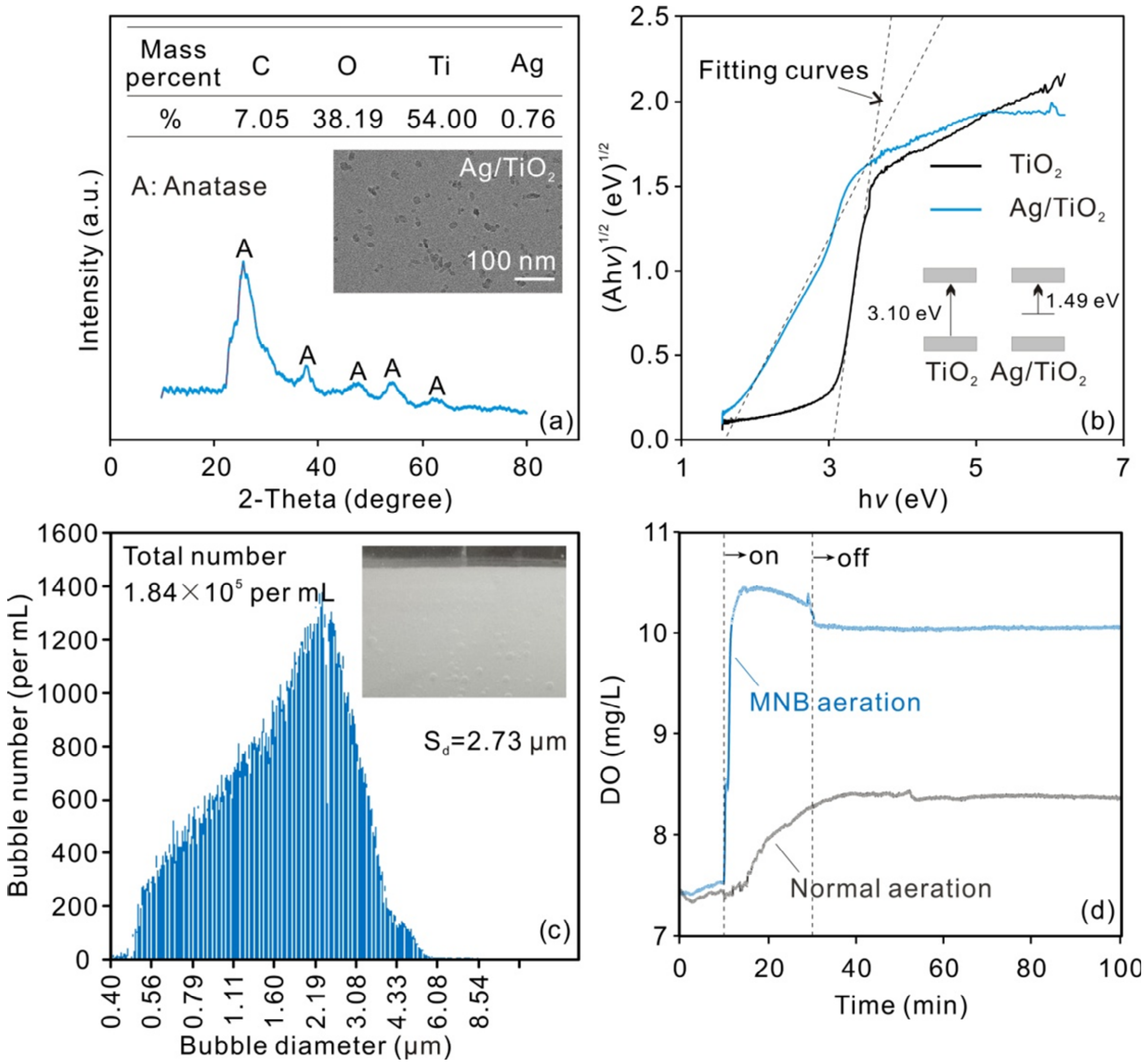

Fig. 2. (a) SEM graaph, EDS result and X-ray diffraction pattern of Ag/TiO_2; (b) Bandgap values obtained from the diffuse reflectance spectra of Ag/TiO_2 and TiO_2; (c) The size and of MNBs in the solution; (d) The DO variations as a function of time in MNB- and normal- aerated water.

3.2. Bactericidal efficiency under visible light photocatalytic disinfection process

The survival rate of the spores (C/C_0) in the MNBs treatment group decreased to 33.3% within 1 h, while the survival rate was 76.9% in the control group (Fig. 3a). In the group with catalyst and MNB but no irradiation, the survival rate was constantly above 98.4% (data not shown). The inactivation rate *k* in the control group (0.23 h^{-1}) without the application of MNBs was consistent with previously reported values (0.06-1.01 h^{-1}) seen during photocatalytic treatment (Sreeja and Shetty, 2016; Obuchi, et al., 2019). However, this study demonstrated that MNBs could facilitate the reaction and resulted in an approximately 5.7 times higher inactivation rate (1.29 h^{-1}).

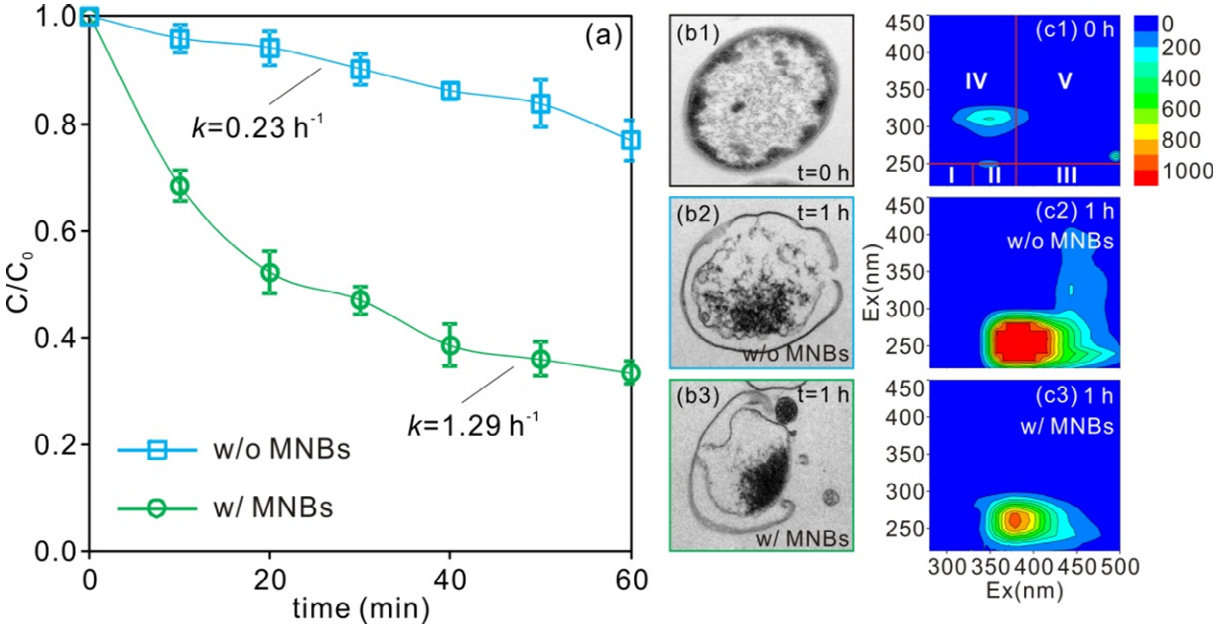

Fig. 3. (a) Comparison between the inactivation capacities of the MNBs treatment (w/ MNBs) and control (w/o MNBs) groups; (b) TEM images of the spores' morphology during the treatment process; (c) EEM spectra of the soluble microbial products in water during the spore inactivation.

TEM images indicated the near-spherical *Bacillus subtilis* spore has a diameter of approximately 880 nm (Fig. 3b1, t=0 h). The untreated spore exhibited a damage-free and well-preserved coat, indicating that the spores were healthy. The reduced integrity of the bacterial spore was a direct indicator of damage to the cellular structure, which has been observed in other photocatalytic treatment processes (Du et al., 2016). In this study, the coats of the spores were destroyed and their shape was deformed by both treatment groups (Fig. 3b2-3). However, the addition of MNBs (Fig. 3b3) clearly induced more severe damage compared with the group without MNBs (Fig. 3b2). The photocatalysis also caused plasmolysis, which prevented observation of the intracellular structures in the micrograph images. This is an effect seen elsewhere during studies on the oxidative destruction of spores (Du et al., 2016; Zhou et al., 2020). Cell debris could also be observed, suggesting the spores suffered considerable damage after the treatment.

The EEM fluorescence spectra analysis was used to illustrate the dynamics of organic substances in the solution during the photocatalytic disinfection process (Fig. 3c1-3). Four fluorescent components were identified, comprising tryptophan-like substances (region II), fulvic-like substances (region III), microbial by-product like substances (region IV), and humic-like substances (region V) (Wang et al., 2021b). Before the treatment (t=0h), only a small amount (relatively low intensity) of soluble microbial by-product like compounds were present in the solution (Fig. 3c1), which may be attributed to the secreted extracellular polymeric substance from the spores (Feng et al., 2020). Along with the photocatalysis process, the cellular structures of spores were damaged (Fig. 3b2-3) and intracellular organic substances could be released from cells (Du et al., 2016). It supports that the tryptophan-like substances, fulvic-like substances, and humic-like substances significantly increased in the treatment group without MNB addition after 1 hour (Fig. 3c2) and in the treatment group with MNB addition after 0.5 hours (Fig. S2). Moreover, such extracellular and release intracellular organic substances are able to be decomposed by photocatalysis (Fan et al., 2019). The fluorescence intensity of all substances in the treatment group with MNBs dramatically reduced to a much lower level after 1 hour (Fig. 3c3) compared with that in the treatment group without MNBs (Fig. 3c3), indicating that the application of MNBs could accelerate the visible light photocatalytic bactericidal process. It is hypothesised that all organic substance would not be identified after a longer treatment period than the current experiment, which should be investigated in further studies.

3.3. The role of ROS in photocatalytic disinfection mechanisms

TiO_2 photocatalysis is a photon-driven reaction process with multiple steps, starting from a photo adsorption event at the surface of the TiO_2 (Fan et al., 2019). When TiO_2 adsorbs photons with energy higher than, or equal to, its bandgap, electrons in the filled valence bands will be excited to the vacant conduction bands, leaving holes in the valence bands. The generation of the electron-hole pair and all ROSs, including h^+, e^-, $\cdot OH$, H_2O_2, and $\cdot O_2^-$, can be descriped in the following reactions (Du et al., 2016; Li et al., 2020):

$$\mathrm{TiO_2} + hv \rightarrow e^- + h^+$$
$$h^+ + \mathrm{H_2O} \rightarrow \cdot\mathrm{OH} + \mathrm{H}^+$$
$$h^+ + \mathrm{OH}^- \rightarrow \cdot\mathrm{OH}$$
$$\mathrm{O_2} + e^- \rightarrow \cdot\mathrm{O_2}^-$$
$$\cdot\mathrm{O_2}^- + \mathrm{H}^+ \rightarrow \mathrm{H_2O}\cdot$$
$$2\mathrm{H_2O}\cdot \rightarrow \mathrm{O_2} + \mathrm{H_2O_2}$$
$$\mathrm{H_2O_2} + \cdot\mathrm{O_2}^- \rightarrow \cdot\mathrm{OH} + \mathrm{OH}^- + \mathrm{O_2}$$

In this study, different scavenging experiments were conducted to identify the key active species responsible for the spores' inactivation. After adding radical scavengers to eliminate the activity of H_2O_2 and ·OH radicals formed during photocatalysis, the survival rates of the spores (C/C_0) significantly increased from 0.33 to 0.86-0.79 in the MNB treatment group and from 0.77 to 0.89-0.88 in the control group MNBs (Fig. 4a). However, the effects of quenching h^+ and $\cdot O_2^-$ on the inactivation of the spores was not significant for both groups, with and without MNBs. It can therefore be concluded that H_2O_2 and ·OH were the primary active species, and the h^+ and $\cdot O_2^-$ took part in the inactivation less intensively. The ·OH has a high redox potential (2.8 eV) but is short-lived, and therefore is unlikely to diffuse further than 1 μm from the TiO_2 surface (Yan et al., 2018). Although H_2O_2 has a weak oxidation capacity (1.78 eV), it is relatively stable with a half-life of several days in water (Clark et al., 2010), which could benefit the permeation of the chemical through the cell wall of the spores. Consequently, the results supported the view that H_2O_2 could work as a spearhead and initially penetrate the cell before damaging the interior structures of the spores. Other ROSs may be involved in damaging the protective coat of the spores and further disrupt the structural integrity once the cell was lysed.

Compared with the results between the two treatment groups, survival rates of the spores (C/C_0) in the MNBs treatment group (0.33-0.86) were always significantly lower compared to those seen for the control group without MNBs (0.77-0.89) (Fig. 4a). The collapse of MNBs has been proposed as a means to directly generate ·OH and $\cdot O_2^-$ (Fan et al., 2019) and may in part explain the improved bactericidal efficiency of the MNB system. However, this is only expected to be observed for very small bubbles in the low nanometre range (Liu et al., 2016), smaller than the bubbles measured here. Instead, the increased treatment efficiency was attributed to the increased transfer of O_2 into the system, as well as the change in the optical characteristics provided by the MNBs.

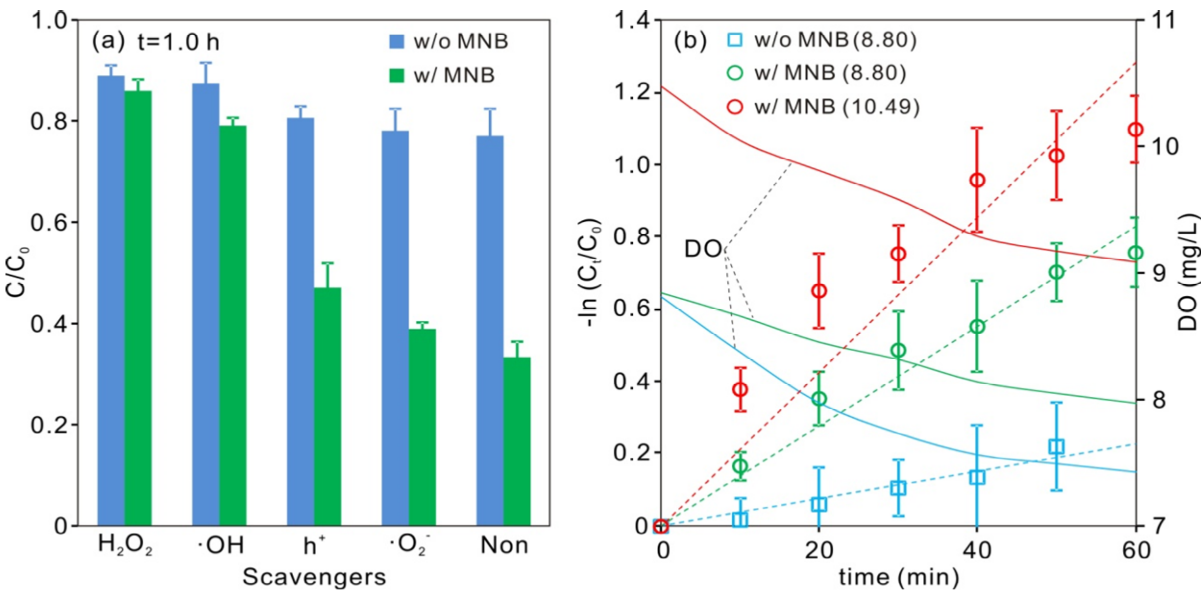

Fig. 4. (a) Photocatalytic disinfection performance of *Bacillus subtilis* spores in the MNBs treatment (w/ MNBs) and control (w/o MNBs) groups in the presence of scavengers (t=1 h). 'Non' denotes no addition of any scavengers. (b) The spores inactivation dynamics and the DO variations in the control (initial DO=8.80 mg/L) and MNBs treatment groups (initial DO=8.80 and 10.49 mg/L, respectively).

3.4. The effect of oxygen from MNBs

It is well known that O_2 can serve as an electron acceptor to generate superoxide radicals and trap electro-generated electrons to mitigate recombination of e^-/h^+ (Kondrakov et al., 2016). Thus, the rate of photocatalysis can be improved by increasing the DO concentration in solution (Liang et al., 2008; Subramanian and Kannan, 2008). The commonly used hydrodynamic cavitation method for MNB generation can induce extra O_2 delivery to water by forming a supersaturated solution (Fig. 2d). This enables sustainable diffusion of O_2 from the long-lasting MNBs. The abovementioned potential contributions of O_2 on the photocatalysis process were investigated separately in the present study. The removal of the spores was higher in the oxygen supersaturated system with MNBs that had an initial DO of 10.49 mg/L (66.7%, k = 1.29 h^{-1}) when compared to the MNBs system at a lower initial DO of 8.80 mg/L (53.1%, k = 0.83 h^{-1}) (Fig. 4b). This agreed with the previous finding that the higher DO level could benefit the treatment. Nevertheless, the supersaturated system is unstable, because of the high vibrational energy of dissolved oxygen molecules and the low entropy (Harano et al., 2018). Once bubble addition was stopped, the oversaturated O_2 is quickly released or consumed and the solution returns to a saturated and stable state (Hirakawa et al., 2007). This helps explain the fast DO reduction by the end of the experiment

(1.40 mg/L) in the supersaturated MNB solution compared with the DO reduction (0.82 mg/L) in the MNB system with lower initial DO.

For the comparison of systems at equivalent initial DO concentration of 8.80 mg/L, the treatment group without MNBs had significantly lower removal of spores (23.1%, k = 0.23 h^{-1}), although the reduction of DO in the group without MNBs (1.39 mg/L) was significantly higher than that (0.82 mg/L) seen in the group with MNBs. As the O_2 in the solution could be continuously replenished by MNBs through inter-bubble gas diffusion (Temesgen et al., 2017), the reduction of the DO level calculated based on instantaneous measurements of the initial and end-state may not be used to explain the difference of the treatment. Moreover, the superior spore inactivation efficiency in the group with MNBs can also be considered to be a combination effects of the increased O_2 supply and the light scattering effect (see section 3.5). However, it was not possible to attribute the contribution of each mechanism.

3.5. Photochemical mechanisms following application of MNBs

The Mie analysis shows the scattering spectra of a single MNB (d=2.73 μm), spore (d=0.88 μm), and Ag/TiO_2 particle (d=22.78 nm) in water drawn in polar plots at an incident wavelength (λ) of 500, 600, and 700 nm (Fig. 5 a-c). Considerable intensity of scattering could be observed in all directions for a single bubble, spore or catalyst particle. Therefore, in the presence of all types of the particle (bubble, spore, and Ag/TiO_2), the light cannot penetrate through the solution in a straight line, and the light propagation becomes defocused (Fan et al., 2021b). The smaller the particle is the variation in the scattering intensity with angle becomes smaller. As the particle becomes larger and the incident wavelength becomes shorter, more scattered light falls in the forward direction (Fig. S3 and S4).

A single Ag/TiO_2 particle has an isotropic intensity distribution and the scattering intensity was much lower than that seen for both the bubble and spore. This was because the nano-sized Ag/TiO_2 fell into the Rayleigh scattering regime (Kim and Chang, 2017) and thus its scattering cross section was the lowest observed (Fig. S5a). Nevertheless, the total relative scattering intensity of the catalyst particles in the test solution was the strongest (Fig. 5d-f) due to it being at the highest concentration, resulting in a high total scattering cross section (Fig. S5b) (Bohren and Huffman, 2008). Therefore, the order of total relative scattering intensity was: total (mixture of MNBs, spores, and Ag/TiO_2 particles), spores and Ag/TiO_2 particles, Ag/TiO_2 particles, MNBs, and spores. When compared to the conventional photocatalytic system (spores and Ag/TiO_2 particles), the addition of MNBs in the ternary system evidently displayed stronger light scattering, which thus prolongs the optical path length in a specific region near to the light source (Fan et al., 2021b). Considering the maximum distance across the photocatalytic reactor between the light source and the water medium was 30 mm, the addition of MNBs into the Ag/TiO_2-spore system increased the total relative scattering intensity by on average 16.6% at a wavelength of 500 nm, 35.6% at $\lambda = 600$ nm, and 54.8% at $\lambda = 700$ nm. Therefore, the MNBs played an important role in increasing the optical path length in the Ag/TiO_2-spore suspension, thus enhancing light adsorption and the photocatalytic reactions in an aqueous solution. These analyses agreed well with the results from the inactivation of spores and the production of ROSs seen in the previous section.

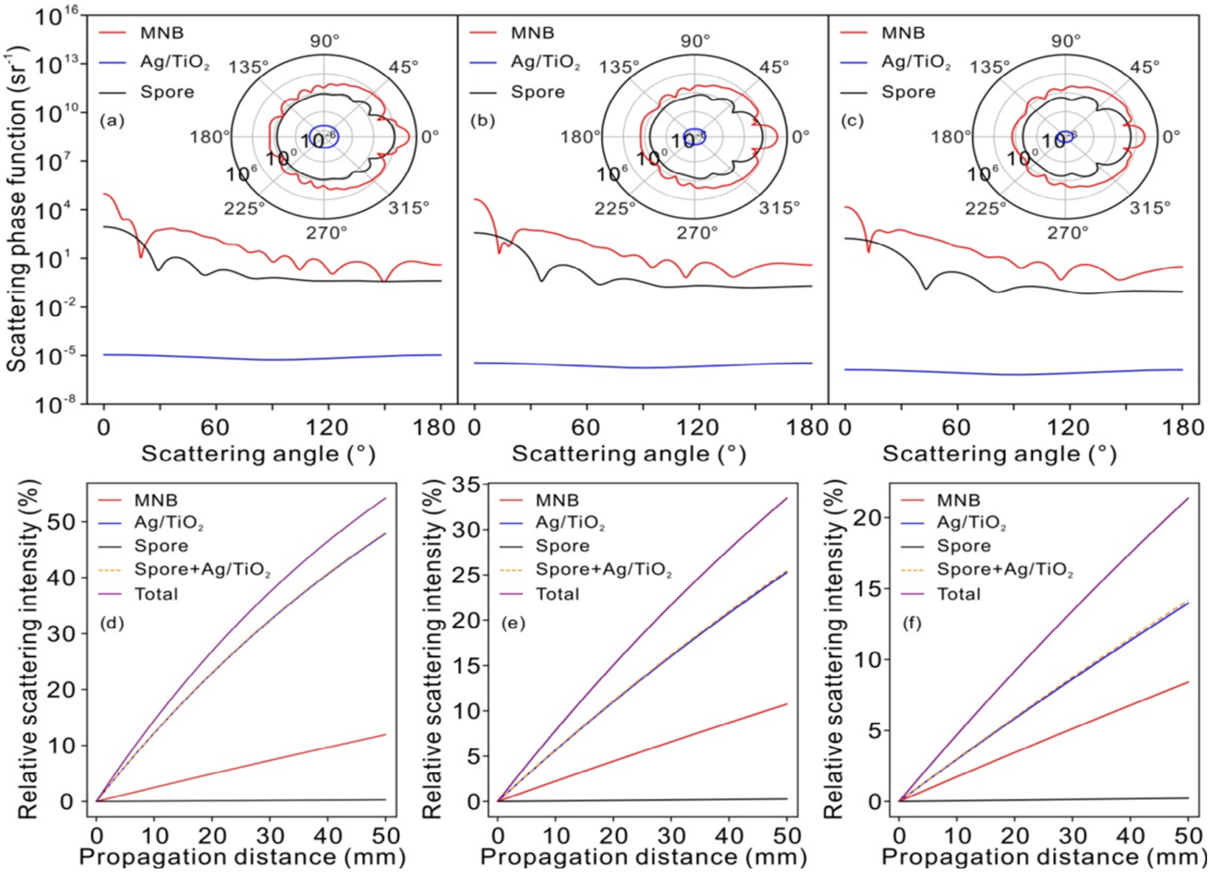

Fig. 5. (a)-(c) The scattering phase function of single bubble, spore and Ag/TiO_2 particle; (d)-(f) The relative scattering intensity at different propagation distances in Ag/TiO_2 suspension, spore suspension,

MNB emulsion, spore+Ag/TiO_2 mixture and the spore -Ag/TiO_2-MNB mixed system (total). (a) and (d): λ = 500 nm, (b) and (e): λ = 600 nm; (c) and (f): λ = 700 nm. In (a)-(c), 0° represents the direction of the incident light, 180° represents the direction of the totally back-scattered light, and all scattered lights at other angles are termed lateral scattering.

The interfacial photoelectric effects of the different particles were verified by the FDTD model. The effect of a single target particle (MNB, Ag/TiO_2 particle and spore) on the propagation of the incident beam at three different wavelengths (500, 600, and 700 nm) is shown in Fig. S6-8. A single MNB had the largest scattering cross-section and the highest scattering intensity, followed by the spore and then the Ag/TiO_2 particle. This was consistent with the Mie analysis (Fig. 5a-c). The near-field distributions of optical intensity for a bubble and a spore adhered to a Ag/TiO_2 particle is illustrated in Fig. 6. When the plane wave arrives at the surface of the bubble or spore, the distribution of the electric field displays a high degree of heterogeneity with periodic oscillation. This is the origin of the angular scattering properties of the MNBs (Fig. 6a-c). In particular, the maximum light intensity in the regions of both the edge of the bubble and in diverged directions is visible. In the presence of MNB, the electric field was enhanced in these regions (Fig. 6d), with the enhancement locally reaching up to 4 times the intensity of incident light compared to the values observed in the absence of MNB (Fig. 6c). If spores coated by Ag/TiO_2 particles locate in these regions with enhanced light intensity, the photocatalytic reaction will be promoted.

In addition to the mechanistic investigations carried out here, it should be noted that the interfacial adsorption of contaminants and/or particles on bubble surfaces is possible (Nguyen et al., 2006). Thus, MNBs may adsorb both spores and Ag/TiO_2 particles in close proximity to the bubble surface, benefiting the performance of the photocatalytic disinfection. However, the contribution of this process was not quantified in the current study, and is an area where further research is required.

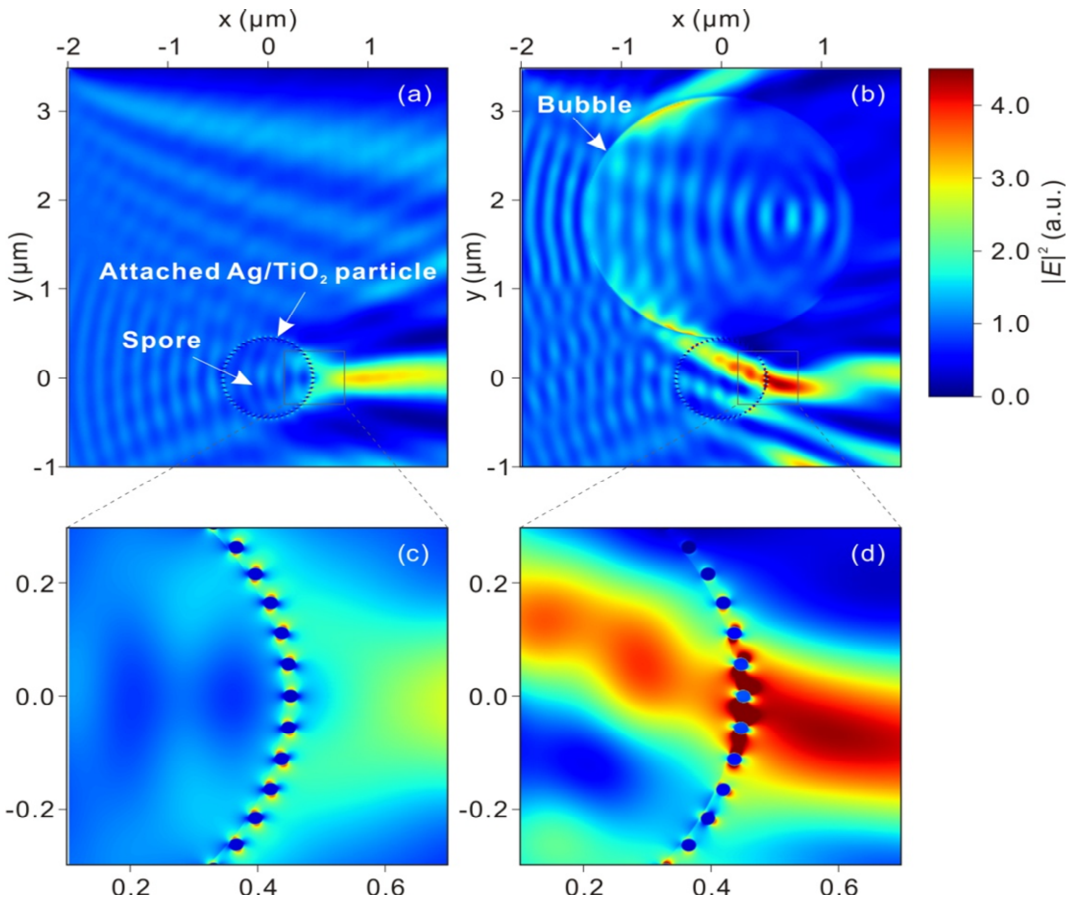

Fig. 6. (a) Electric field distribution near an illuminated spore with attached Ag/TiO_2 particles. The incident wavelength is 500 nm. (b) Electric field distribution near an illuminated MNB with a nearby Ag/TiO_2 particles coated spore. (c) and (d) are the enlarged images for certain positions of (a) and (b), respectively.

3.6. Implementation potential

Photocatalysis, as an advanced oxidation technique, has been the subject of extensive research over recent decades. However, this technology is not widely used operationally because of its low efficiency. This is explained by the enhancement of the process at high energy short wavelengths of light, fast charge recombination, and low migration of the photo-generated electrons and holes into the bulk solution (Koe et al., 2020). The current study demonstrated that MNBs can enrich the oxygen content in aqueous solution and increase the light absorption of photocatalysts, consequently the photocatalytic disinfection could be significantly enhanced. In order to implement practical applications and upgrade the water disinfection facilities, the MNBs approach could be effectively incorporated into current widely used photocatalytic units, such as fixed-bed reactors (Fig. S9a). The applied fine photocatalyst particles (Ag/TiO_2) can be immobilized onto a solid support matrix, for example glass beads, zeolite or directly onto membranes, enabling easy separation and reuse of the photocatalysts (McCullagh et al., 2011). The MNB can be applied directly into the water prior to entering the photocatalytic units, enabling stable performance. An alternative approach is to apply the photocatalysts and MNBs directly into contaminated water sources, taking advantage of natural solar irradiation. In this concept, floating photocatalysts using self-buoyant media or low density carriers, have been applied on the surface of natural waters to decompose cyanobacteria, antibiotics, and toxic metals (Fig. S9b) (Xing et al., 2018). MNB technology has recently been introduced into natural waters for water and sediment remediation in eutrophic waters (Zhang et al., 2018). Combining MNBs with photocatalysis is therefore expected to provide synergetic effects on *in-situ* natural water remediation with a large specific surface area (Fig. S9b).

While the present study demonstrates the feasibility of MNB photocatalysis for disinfection applications, it is expected that this will translate to oxidation of chemical pollutants, including organic micropollutants. MNBs have also been postulated to generate free radicals during bubble collapse which may additionally contribute to enhanced oxidation reactions, potentially facilitating degradation of a broad range of contaminants with and without photocatalysts being present (Liu et al., 2016; Fan et al., 2019). Nevertheless, given the complexity of light propagation, photochemical reactions and bubble dynamics in real water bodies, further study on the impacts of background matrix and hydraulics on the efficiency of MNB-assisted photocatalysis processes is needed for disinfection and oxidation applications.

4. Conclusions

Our study has demonstrated that micro/nano bubble (MNBs) can act as a chemical free additive to enhance the disinfection capability of the conventional visible light photocatalytic process. The inactivation efficiency of *Bacillus subtilis* spores with MNBs present was significantly higher than that in the system without MNBs. The H_2O_2 and $\cdot OH$ were the primary ROSs that contributed to the disinfection processes. The presence of MNBs provided a sustainable oxygen supply to activate the hole oxidation by capturing photoelectrons, and inducing strong light scattering to increase the optical path length in the solution. Meanwhile, the dielectric change at the bubble-solution interface leads to 'high-degree' heterogeneity of the electric field, resulting from the formation of regions with enhanced light intensity, where the photocatalytic reactions can be promoted. Notably, the current research was conducted over one-hour photocatalysis experiments. Longer-term continuous experiments and upscaled reactor configurations should be investigated in order to move towards full-scale application of the process. This will enable a full cost-benefit analysis of the process to be carried out. Nevertheless, this study opens up new prospects for the development of photocatalysis coupled with MNBs for advanced water treatment.

Credit author statement

Wei Fan: Methodology, Investigation, Writing-Original Draft. **Jingyu Cui**: Methodology, Investigation. **Qi Li**: Investigation, Formal analysis. **Yang Huo**: Methodology, Visualization. **Dan Xiao**: Software, Visualization. **Xia Yang**: Software. **Hongbin Yu**: Formal analysis. **Chunliang Wang**: Methodology, Supervision. **Peter Jarvis**: Writing-Review & Editing. **Tao Lyu**: Writing-Review & Editing, Conceptualization. **Mingxin Huo**: Resources.

Acknowledgments

This work was funded by the National Natural Science Foundation of China (51978135, 51678121, 51478095, and 51878133). It was also supported by the Scientific and Technological Development Plan Project of Jilin Province (No. 20200201042JC).

References

Almquist, C.B., Biswas, P., 2001. A mechanistic approach to modeling the effect of dissolved oxygen in photo-oxidation reactions on titanium dioxide in aqueous systems. Chem. Eng. Sci. 56, 3421-3430. https://doi.org/10.1016/S0009-2509(01)00045-8.

Athanasiou, D.A., Romanos, G. E., Falaras, P., 2016. Design and optimization of a photocatalytic reactor for water purification combining optical fiber and membrane technologies. Chem. Eng. J. 305, 92-103. https://doi.org/10.1016/j.cej.2015.11.080.

Bohren, C.F. and Huffman, D.R., 2008. Absorption and scattering of light by small particles. John Wiley & Sons.

Chen, L., Xu, Y., Chen, B., 2019. In situ photochemical fabrication of CdS/g-C_3N_4 nanocomposites with high performance for hydrogen evolution under visible light. Appl. Catal. B 256, 117848. https://doi.org/10.1016/j.apcatb.2019.117848.

Choi, Y., Cho, M., Lee, Y., Choi, J., Yoon, J., 2007. Inactivation of Bacillus subtilis spores during ozonation in water treatment plant: Influence of pre-treatment and consequences for positioning of the ozonation step. Chemosphere 69, 675-681. https://doi.org/10.1016/j.chemosphere.2007.05.045.

Churnside, J.H., 2010. Lidar signature from bubbles in the sea. Opt. Express 18, 8294-8299. https://doi.org/10.1364/OE.18.008294.

Clark, C.D., Bruyn, W.J., Hirsch, C.M., Jakubowski, S.D., 2010. Hydrogen peroxide measurements in recreational marine bathing waters in Southern California, USA. Water Res. 44, 2203-2210. https://doi.org/10.1016/j.watres.2009.12.044.

Dalrymple, O.K., Stefanakos, E., Trotz, M.A., Goswami, D.Y., 2010. A review of the mechanisms and modeling of photocatalytic disinfection. Appl. Catal. B 98, 27-38. https://doi.org/10.1016/j.apcatb.2010.05.001.

Ding, W., Jin, W., Cao, S., Zhou, X., Wang, C., Jiang, Q., Huang, H., Tu, R., Han, S., Wang, Q., 2019. Ozone disinfection of chlorine-resistant bacteria in drinking water. Water Res. 160, 339-349. https://doi.org/10.1016/j.watres.2019.05.014.

Du, Y., Xiong, H., Dong, S., Zhang, J., Ma, D., Zhou, D., 2016. Identifying the role of reactive oxygen species (ROSs) in Fusarium solani spores inactivation, AMB Express. 6, 81. https://doi.org/10.1186/s13568-016-0257-1.

Fan, W., Zhou, Z., Wang, W., Huo, M., Zhang, L., Zhu, S., Yang, W., Wang, X., 2019. Environmentally friendly approach for advanced treatment of municipal secondary effluent by integration of micro-nano bubbles and photocatalysis. J. Clean. Prod. 237, 117828. https://doi.org/10.1016/j.jclepro.2019.117828.

Fan, W., An, W., Huo, M., Yang, W., Zhu, S., Lin, S., 2020. Solubilization and stabilization for prolonged reactivity of ozone using micro-nano bubbles and ozone-saturated solvent: A promising enhancement for ozonation. Sep. Purif.Technol. 238, 116484. https://doi.org/10.1016/j.seppur.2019.116484.

Fan, W., An, W., Huo, M., Xiao, D., Lyu, T., Cui, J., 2021a. An integrated approach using ozone nanobubble and cyclodextrin inclusion complexation to enhance the removal of micropollutants. Water Res. 196, 117309. https://doi.org/10.1016/j.watres.2021.117039.

Fan, W., Desai, P., Zimmerman, W.B., Duan, Y., Crittenden, J.C., Wang, C., Huo, M., 2021b. Optical density inferences in aqueous solution with embedded micro/nano bubbles: A reminder for the emerging green bubble cleantech. J. Clean. Prod. 294, 126258. https://doi.org/10.1016/j.jclepro.2021.126258.

Feng, X., Wu, Q., Che, L., Ren, N., 2020. Analyzing the inhibitory effect of metabolic uncoupler on bacterial initial attachment and biofilm development and the underlying mechanism. Environ. Res. 185, 109390. https://doi.org/10.1016/j.envres.2020.109390.

Friedline, A., Zachariah, M., Middaugh, A., Heiser, M., Khanna, N., Vaishampayan, P., Rice, C.V., 2015. Sterilization of hydrogen peroxide resistant bacterial spores with stabilized chlorine dioxide. AMB Express, 5, 24. https://doi.org/10.1186/s13568-015-0109-4.

Harano, F.K.F., Ferreira, M. S., Mateus, M.V., Ferreira, D.C., Gonçalves, J.C.S.I., 2018. Reaeration and oxygen dissipation into a circular hydraulic channel: experimental and dimensionless approach. Braz. J. Water Res. 23, e12. https://doi.org/10.1590/2318-0331.231820170138.

Hirakawa, T., Daimon, T., Kitazawa, M., Ohguri, N., Koga, C., Negishi, N., Matsuzawa, S., Nosaka, Y., 2007. An approach to estimating photocatalytic activity of TiO_2 suspension by monitoring dissolved oxygen and superoxide ion on decomposing organic compounds. J. Photoch. Photobio. A. 190, 58-68. https://doi.org/10.1016/j.jphotochem.2007.03.012.

Hu, W., Yang, S., Yang, S., 2020. Surface modification of TiO_2 for perovskite solar cells. Trends in Chemistry , 148-162. https://doi.org/10.1016/j.trechm.2019.11.002.

Jiang, L., Yuan, X., Pan, Y., Liang, J., Zeng, G., Wu, Z., Wang. H., 2017. Doping of graphitic carbon nitride for photocatalysis: A review. Appl. Catal. B 217, 388-406. https://doi.org/10.1016/j.apcatb.2017.06.003.

John, A., Brookes, A., Carra, I., Jefferson, B. Jarvis, P., 2020. Microbubbles and their application to ozonation in water treatment: A critical review exploring their benefit and future application. Crit. Rev. Environ. Sci. Technol. https://doi.org/10.1080/10643389.2020.1860406 .

Jung, Y.J., Oh, B.S., Kang, J.W., 2008. Synergistic effect of sequential or combined use of ozone and UV radiation for the disinfection of Bacillus subtilis spores. Water Res. 42, 1613-1621. https://doi.org/10.1016/j.watres.2007.10.008.

Kim, H., Chang, J.H., 2017. Increased light penetration due to ultrasound-induced air bubbles in optical scattering media. Sci. Rep. 7, 16105. https://doi.org/10.1038/s41598-017-16444-9.

Koe, W.S., Lee, J.W., Chong, W.C., Pang, L.Y., Sim, L.C., 2020. An overview of photocatalytic degradation: photocatalysts, mechanisms, and development of photocatalytic membrane. Environ. Sci. Pollut. Res. Int. 27, 2522-2565. https://doi.org/10.1007/s11356-019-07193-5.

Kondrakov, A.O., Ignatev, A.N., Lunin, V.V., Frimmel, F.H., Bräse, S., Horn, H., 2016. Roles of water and dissolved oxygen in photocatalytic generation of free OH radicals in aqueous TiO_2 suspensions: An isotope labeling study. Appl. Catal. B 182, 424-430. https://doi.org/10.1016/j.apcatb.2015.09.038.

Lee, M.S., Hong, S.S., Mohseni, M., 2005. Synthesis of photocatalytic nanosized TiO_2-Ag particles with sol-gel method using reduction agent, J. Mol. Catal. A-Chem. 242, 135-140. https://doi.org/10.1016/j.molcata.2005.07.038.

Leggett, M.J., McDonnell, G., Denyer, S.P., Setlow, P., Maillard, J.Y., 2012. Bacterial spore structures and their protective role inbiocide resistance. J. Appl. Microbiol. 113, 485-498. https://doi.org/10.1111/j.1365-2672.2012.05336.x.

Li, H., Sun, S., Ji, H., Liu, W., Shen Z., 2020. Enhanced activation of molecular oxygen and degradation of tetracycline over Cu-S4 atomic clusters. Appl. Catal. B. 272, 118966. https://doi.org/10.1016/j.apcatb.2020.118966.

Li, Q., Yang, J., Fan, W., Zhou, D., Wang, X., Zhang, L., Huo, M., Crittenden, J.C., 2018. Different transport behaviors of Bacillus subtilis cells and spores in saturated porous media: Implications for contamination risks associated with bacterial sporulation in aquifer. Colloids Surf. B 162, 35-42. https://doi.org/10.1016/j.colsurfb.2017.11.018.

Liang, H., Li, X., Yang, Y., Sze, K., 2008. Effects of dissolved oxygen, pH, and anions on the 2,3-dichlorophenol degradation by photocatalytic reaction with anodic TiO_2 nanotube films. Chemosphere 73, 805-812. https://doi.org/10.1016/j.chemosphere.2008.06.007.

Lim, J.B., Langford, T.F., Huang, B.K., Deen, W.M., Sikes, H.D., 2016. A reaction-diffusion model of cytosolic hydrogen peroxide, Free Radic. Biol. Med. 90, 85-90. https://doi.org/10.1016/j.freeradbiomed.2015.11.005.

Liu, S, Oshita, S., Kawabata, S., Makino, Y. & Yoshimoto, T. (2016). Identification of ROS produced by nanobubbles and their positive and negative effects on vegetable seed germination. Langmuir, 32, 11295-11302. https://doi.org/10.1021/acs.langmuir.6b01621.

Lyu, T., Wu, S., Mortimer, R.J.G., Pan, G., 2019. Nanobubble technology in environmental engineering: revolutionization potential and challenges. Environ. Sci. Technol. 53, 7175-7176. https://doi.org/10.1021/acs.est.9b02821.

McCullagh, C., Skillen, N., Adams, M., Robertson, P.K.J., 2011. Photocatalytic reactors for environmental remediation: A review. J. Chem. Technol. Biotechnol. 86, 1002-1017. https://doi.org/10.1002/jctb.2650.

McGivney, E., Han, L., Avellan, A., VanBriesen, J., Gregory, K.B., 2017. Disruption of autolysis in *Bacillus subtilis* using TiO_2 Nanoparticles, Sci. Rep. 7, 44308. https://doi.org/10.1038/srep44308.

Nguyen, A.V., Phan, C.M., Evans, G.M., 2006. Effect of the bubble size on the dynamic adsorption of frothers and collectors in flotation. Int. J. Miner. Process 79, 18-26. https://doi.org/10.1016/j.minpro.2005.11.007.

Obuchi, E., Furusho, T., Katoh, T., Katoh, K., Soejima, T., Nakano, K., 2019. Photocatalytic disinfection of sporulating Bacillus subtilis using silver-doped TiO_2/SiO_2. J. Water Process Eng. 30, 100511. https://doi.org/10.1016/j.jwpe.2017.10.011.

Parangi, T., Mishra, M.K., 2019. Titania nanoparticles as modified photocatalysts: a review on design and development. Comment Inorg. Chem. 39, 90-126. https://doi.org/10.1080/02603594.2019.1592751.

Phaniendra, A., Jestadi, D.B., Periyasamy, L., 2015. Free radicals: properties, sources, targets, and their implication in various diseases. Indian J. Clin. Biochem. 30, 11-26. https://doi.org/10.1007/s12291-014-0446-0.

Sella, S.R.B.R., Vandenberghe, L.P.S., Soccol, C.R., 2014. Life cycle and spore resistance of spore-forming Bacillus atrophaeus. Microbiol. Res. 169, 931-939. https://doi.org/10.1016/j.micres.2014.05.001.

Setlow, P., 2014. Spore resistance properties, Microbiol. Spectr. 2, 1-14. https://doi.org/10.1128/microbiolspec.TBS-0003-2012.

Setlow, B., Loshon, C.A., Genest, P.C., Cowan, A.E., Setlow, C., Setlow, P., 2002. Mechanisms of killing spores of Bacillus subtilis by acid, alkali and ethanol. J. Appl. Microbiol. 92, 362-375. https://doi.org/10.1046/j.1365-2672.2002.01540.x.

Sreeja, S., Shetty, K.V., 2016. Microbial disinfection of water with endotoxin degradation by photocatalysis using Ag@TiO_2 core shell nanoparticles. Environ. Sci. Pollut. Res. Int. 23, 18154-18164. https://doi.org/10.1007/s11356-016-6841-8.

Subramanian, M., Kannan, A., 2008. Effect of dissolved oxygen concentration and light intensity on photocatalytic degradation of phenol. Korean J. Chem. Eng. 25, 1300-1308. https://doi.org/10.1007/s11814-008-0213-0.

Sumlin, B.J., Heinson, W.R., Chakrabarty, R.K., 2018. Retrieving the aerosol complex refractive index using PyMieScatt: A Mie computational package with visualization capabilities. J. Quant. Spectrosc. Ra. 205, 127-134. https://doi.org/10.1016/j.jqsrt.2017.10.012.

Temesgen, T., Bui, T.T., Han, M., Kim, T., Park, H., 2017. Micro and nanobubble technologies as a new horizon for water-treatment techniques: a review. Adv. Colloid Interfac. 246, 40-51. https://doi.org/10.1016/j.cis.2017.06.011.

Wang, S., Liu, Y., Lyu, T., Pan, G., Li, P., 2021a. Aquatic macrophytes in morphological and physiological responses to the nanobubble technology application for water restoration. ACS EST

Water 1, 376-387. https://doi.org/10.1021/acsestwater.0c00145.
Wang, W., Fan, W., Huo, M., Zhao, H., Lu. Y., 2018. Hydroxyl radical generation and contaminant removal from water by the collapse of microbubbles under different hydrochemical conditions. Water Air Soil Pollut. 229, 86. https://doi.org/10.1007/s11270-018-3745-x.
Wang, X., Muhmood, A., Lyu, T., Dong, R., Liu, H., Wu, S., 2021b. Mechanisms of genuine humic acid evolution and its dynamic interaction with methane production in anaerobic digestion processes. Chem. Eng. J. 408, 127322. https://doi.org/10.1016/j.cej.2020.127322.
Wassmann, M., Moeller, R., Rabbow, E., Panitz, C., Horneck, G., Reitz, G., Douki, T., Cadet, J., Stan-Lotter, H., Cockell, C.S., Rettberg, P., 2012. Survival of spores of the UV-resistant Bacillus subtilis Strain MW01 after exposure to low-earth orbit and simulated martian conditions: data from the space experiment ADAPT on EXPOSE-E. Astrobiology, 12, 498-507. https://doi.org/10.1089/ast.2011.0772.
Wriedt, T., 2012. Mie Theory: A Review. In: Hergert W., Wriedt T. (eds) The Mie Theory. Springer Series in Optical Sciences, 169. Springer, Berlin, Heidelberg. https://doi.org/10.1007/978-3-642-28738-1_2.
Wu, Y., Lyu, T., Yue, B., Tonoli, E., Verderio, E.A.M., Ma, Y., Pan, G., 2019. Enhancement of tomato plant growth and productivity in organic farming by agri-nanotechnology using nanobubble oxygation. J. Agric. Food Chem. 67, 10823-10831. https://doi.org/10.1021/acs.jafc.9b04117.
Xia, D., Shen, Z., Huang, G., Wang, W., Yu, J.C., Wong, P.K., 2015. Red Phosphorus: an earth-abundant elemental photocatalyst for "green" bacterial inactivation under visible light. Environ. Sci. Technol. 49, 6264-6273. https://doi.org/10.1021/acs.est.5b00531.
Xin Z., Zhao, X., Ji, H., Ma, T., Li, H., Zhong, S., Shen, Z., 2020. Amorphous carbon-linked TiO_2/carbon nanotube film composite with enhanced photocatalytic performance: The effect of interface contact and hydrophilicity. Chinese Chem. Lett. https://doi.org/10.1016/j.cclet.2020.11.054.
Xing, M., Li, X., Zhang, J., 2014. Synergistic effect on the visible light activity of Ti^{3+} doped TiO_2 nanorods/boron doped graphene composite. Sci. Rep. 4, 5493. https://doi.org/10.1038/srep05493.
Xing, Z., Zhang, J., Cui, J., Yin, J., Zhao, T., Kuang, J., Xiu, Z., Wan, N., Zhou, W., 2018. Recent advances in floating TiO_2-based photocatalysts for environmental application. Appl. Catal. B 225, 452-467. https://doi.org/10.1016/j.apcatb.2017.12.005.
Yan, Y., Zhou, X., Lan, J., Li, Z., Zheng, T., Cao, W., Zhu, N., Liu, W., 2018. Efficient photocatalytic disinfection of Escherichia coli by N-doped TiO_2 coated on coal fly ash cenospheres. J. Photochem. Photobiol. A 367, 355-364. https://doi.org/10.1016/j.jphotochem.2018.08.045
Zhang, H., Lyu, T., Bi, L., Tempero, G., Hamilton, D.P., Pan, G., 2018. Combating hypoxia/anoxia at sediment-water interfaces: A preliminary study of oxygen nanobubble modified clay materials. Sci. Total Environ. 637-638, 550-560. https://doi.org/10.1016/j.scitotenv.2018.04.284.
Zhang, X.H., Maeda, N., Craig, V.S.J., 2006. Physical properties of nanobubbles on hydrophobic surfaces in water and aqueous solutions. Langmuir 22, 5025-5035. https://doi.org/10.1021/la0601814.
Zhong, Y., Gan, W., Du, Y., Huang, H., Wu, Q., Xiang, Y., Shang, C., Yang, X., 2019. Disinfection byproducts and their toxicity in wastewater effluents treated by the mixing oxidant of ClO_2/Cl_2. Water Res. 162, 471-481. https://doi.org/10.1016/j.watres.2019.07.012.
Zhou, Z., Shen, Z., Cheng, Z., Zhang, G., Li, M., Li, Y., Zhan, S., Crittenden, J.C., 2020. Mechanistic insights for efficient inactivation of antibiotic resistance genes: a synergistic interfacial adsorption

and photocatalytic-oxidation process. Sci. Bull. 65, 2107-2119. https://doi.org/10.1016/j.scib.2020.07.015.

Supplementary Material

Bactericidal efficiency and photochemical mechanisms of micro/nano bubble–enhanced visible light photocatalytic water disinfection

Wei Fan [a], Jingyu Cui [a], Qi Li [a], Yang Huo [b], Dan Xiao [c], Xia Yang [a], Hongbin Yu [a], Chunliang Wang [b,*], Peter Jarvis [d], Tao Lyu [d,*], Mingxin Huo [a]

[a] *School of Environment, Northeast Normal University, 2555 Jingyue Street, Changchun, 130117, China*

[b] *National Demonstration Center for Experimental Physics Education, Northeast Normal University, Changchun 130024, China*

[c] *Jilin Academy of Agricultural Science, 1363 Shengtai Street, Changchun, 130033, China*

[d] *Cranfield Water Science Institute, Cranfield University, College Road, Cranfield, Bedfordshire, MK43 0AL, UK*

Corresponding authors: wangclnenu@163.com (C.W.). t.lyu@cranfield.ac.uk (T.L.)

The following supplementary material follows the chronological sequence structure of the information mentioned in the main text.

S1. Mie analysis of light scattering induced by MNB

According to classical electromagnetic theory, light scattering of a bubble triggered by charge excitation or re-radiation of the electromagnetic energy was schematically illustrated in Fig. 1. The scattering is identical at all polar angles φ, while the distribution of the scattered intensities $F(\theta,\varphi)$ at different angles θ has great influence on the light propagation. The ultrafine MNBs with high inner pressure in water usually tend to be spherical, and the bubble size in this study was comparable to the light wavelength. Mie theory was thus applied to calculate the scattering properties, which provided an analytical solution of Maxwell's equations for the scattering of electromagnetic radiation by spherical particles in terms of infinite series (Wriedt, 2012). For unpolarized incident light, since the scattered energy in the far-field is $I_s \propto |S_1|^2 + |S_2|^2$, the $F(\theta,\varphi)$ and the relative scattering intensity (R_{scat}) at different propagation distance (z) can be derived as (Wriedt, 2012; Sumlin et al., 2018)

$$I_s(\alpha) = \frac{\lambda^2}{8\pi^2 R^2} I_0(|S_1|^2 + |S_2|^2) \qquad (1)$$

$$F(\alpha,\beta) = \frac{1}{2}(|S_1|^2 + |S_2|^2) \qquad (2)$$

$$P(\cos\alpha) = \frac{4F(\alpha,\beta)}{k^2 \pi d^2 Q_{sca}} \qquad (3)$$

$$Q_{sca} = \frac{2}{k^2}\sum_{n=1}^{\infty}(2n+1)(|a_n|^2 + |b_n|^2) \qquad (4)$$

$$S_1 = \sum_{n}^{n_{max}} \frac{2n+1}{n(n+1)}(a_n \pi_n + b_n \tau_n) \qquad (5)$$

$$S_1 = \sum_{n}^{n_{max}} \frac{2n+1}{n(n+1)}(a_n \tau_n + b_n \pi_n) \qquad (6)$$

where, $I_s(\alpha)$ is the intensity of scattering light at the point P with distance R from the bubble center; λ is the wavelength of incident light (Fig. S1); S_1 and S_2 are the amplitude functions; Q_{sca} is scattering efficiencies; a_n and b_n are the Mie coefficients. π_n and τ_n are all functions of scattering angle, which are calculated from recurrence relations. Calculations were performed with the Mie computational package PyMieScatt (Sumlin et al., 2018). For a spherical air bubble, the refractive index was set as n_{air}=1 while n_{water}=1.33, n_{spore}=1.52, and $n_{Ag/TiO2}$=2.50.

In a bubbly emulsion, a light beam will be continuously scattered as it propagates in liquid with identical scattering bubbles. For a small propagation distance Δz, the scattered light intensity can be written as

$$\Delta I = I(z) \cdot \rho \cdot \sigma_s \cdot \Delta z \qquad (7)$$

where ρ is the concentration of the scattering bubbles, and σ_s is the scattering cross section of each bubble which can be calculated using PyMieScatt. As the propagation distance z increases, more light is scattered. Assuming the initial intensity of the incident beam is I_0, the scattered intensity ($I_{scat}(z)$) and relative scattering intensity (R_{scat}) at the propagation length z can be written as

$$\begin{cases} I_{scat}(z) = I_0 \cdot [1 - \exp(-\rho\sigma_s z)] \\ R_{scat} = I_{scat}(z) / I_0 = [1 - \exp(-\rho\sigma_s z)] \times 100\% \end{cases} \qquad (8)$$

S2. Finite-difference time-domain (FDTD) modeling

As the sizes of MNBs, spores, and Ag/TiO_2 particles were in the μm and nm ranges, the local optical field intensity around them was an important factor of the optical excitation. The MNBs can not only induce macro scatterings, but also modify the near field distribution of the optical field. For this scattering process, far-field scattering originates from the near-field properties. The interfered electric field near the bubble was calculated using the finite-difference time-domain (FDTD) method (Chowdhury et al., 2008; Oskooi et al., 2010). The FDTD method discretizes Maxwell's time-dependent curl equations using central-difference approximations for the space and time partial derivatives of the electric and magnetic fields.

In the FDTD method, the evolution of the electromagnetic fields is simulated by solving the following Maxwell's time-dependent curl equations (Bohren and Huffman, 2004):

$$\begin{aligned} \nabla \times \vec{E} &= -\frac{\partial \vec{B}}{\partial t} \\ \vec{B} &= \mu * \vec{H} \\ \nabla \times \vec{H} &= \frac{\partial \vec{D}}{\partial t} \\ \vec{D} &= \varepsilon * \vec{E} \end{aligned} \qquad (9)$$

where $\vec{E}$ and $\vec{H}$ are electric and magnetic fields, respectively. ε and μ denote the permittivity and permeability, $\vec{D}$ and $\vec{B}$ represent the electric displacement field and magnetic flux density. The simulated area is finely divided into spatial grids in Cartesian coordinates. In each grid cell, the partial differential equations are solved using central-difference approximations. After the pulsed stimulation of an electromagnetic wave source, the fields in the simulated area are updated in small time steps. The properties of fields in the frequency domain can be obtained by the Fourier Transform of the transient response. Therefore, the amplitude of sinusoidal electric fields ($|\vec{E}|$) can be calculated at certain frequencies.

A schematic representation of the 2D FDTD computational domain is shown in Figure S1. A plane-wave was set to propagate toward the y axis, and the polarization was set to be in the x direction (Fig. S1). A field and power monitor in the frequency domain was used to record the electrical intensity ($|E|^2$, representing the optical intensity). The simulated area was set to be 4.8 μm×5.5 μm, which was large enough to see the near field properties around the spore, MNB, and Ag/TiO_2 particle. The final monitoring domain shown in Fig. S1 was $-2\mu m \le x \le 1.8\mu m$ and $-1\mu m \le y \le 3.5\mu m$. The simulation area was surrounded by perfect matched layers (PML), which absorbed all the electromagnetic waves reaching the simulation boundaries, so that there was no unwanted reflection left. Three scenarios of FDTD modeling were simulated: (1) water alone; (2) single MNB, single spore, and single Ag/TiO_2 particle; (3) Fifty Ag/TiO_2 particles were placed at the surface of the spore, and An MNB was placed closely to the spore. Since the optical intensity *I* is proportional to the square of the amplitude of the oscillating electric field $|E|^2$, the electric field distribution in the simulation area was recorded in the frequency domain. The relative intensity of $|E|^2$ at different positions was denoted by different colors. Colors ranging from blue to red represented intensities that ranged from weak to strong. The diameters of the bubble, spore and the Ag/TiO_2 particle were set to the tested average values in photocatalytic experiments. The interfacial photoelectric effects induced by the MNBs could be obtained by comparing the different scenarios.

References

Bohren, C.F., Huffman, D.R., 2004. Absorption and scattering of light by small particles. Wiley VCH. Weinheim.

Sumlin, B.J., Heinson, W.R., Chakrabarty, R.K., 2018. Retrieving the aerosol complex refractive index using PyMieScatt: A Mie computational package with visualization capabilities. J. Quant. Spectrosc. Ra. 205, 127-134. https://doi.org/10.1016/j.jqsrt.2017.10.012.

Wriedt, T., 2012. Mie Theory: A Review. In: Hergert W., Wriedt T. (eds) The Mie Theory. Springer Series in Optical Sciences, 169 (2012). Springer, Berlin, Heidelberg. https://doi.org/10.1007/978-3-642-28738-1_2.

Oskooi, A.F., Roundy, D., Ibanescu, M., Bermel, P., Joannopoulos, J.D., Johnson, S.G., 2010. Meep: A flexible free-software package for electromagnetic simulations by the FDTD method. Comput. Phys. Commun. 181(3). https://doi.org/10.1016/j.cpc.2009.11.008.

Chowdhury, M.H., Pond, J., Gray, S.K., Lakowicz, J.R., 2008. Systematic computational study of the effect of silver nanoparticle dimers on the coupled emission from nearby fluorophores. J. Phys. Chem. C. 112(30)11236-11249. https://doi.org/10.1021/jp802414k.

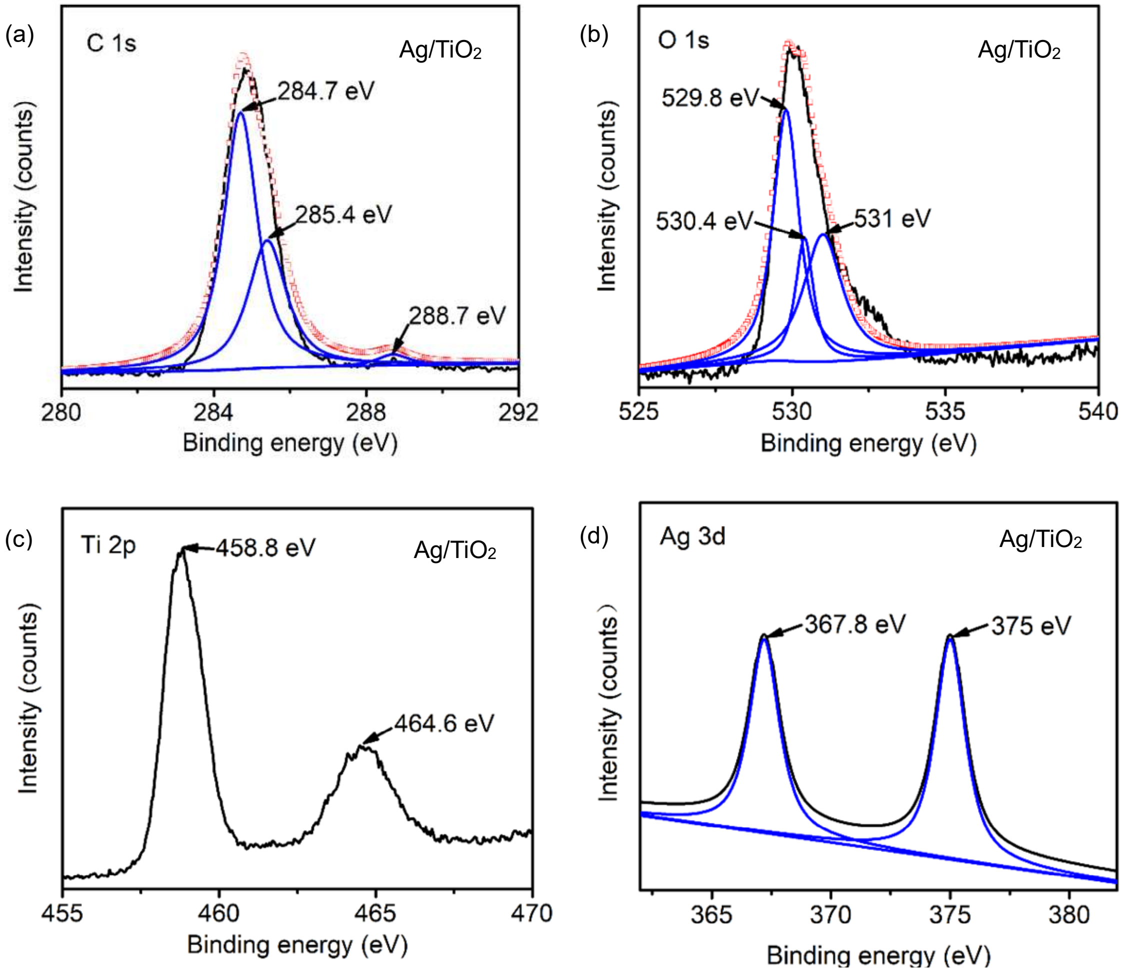

Fig. S1 High resolution XPS spectra of C1s, O1s, Ti 2p, and Ag 3d in Ag/TiO_2 sample.

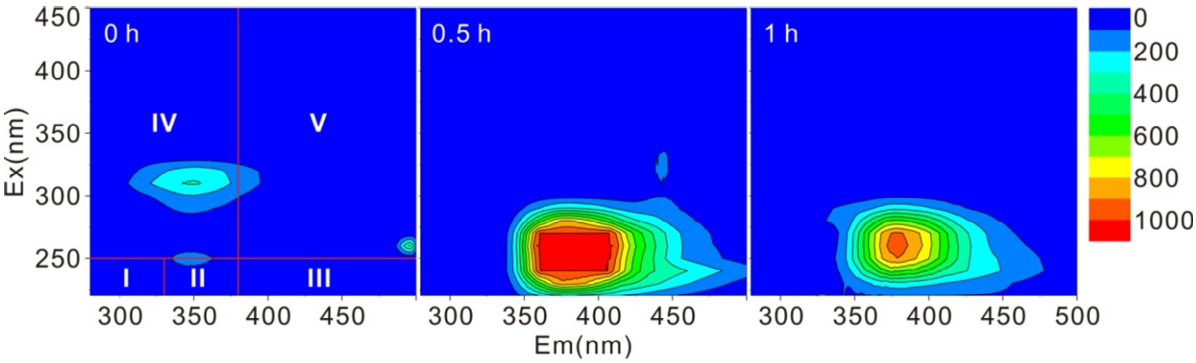

Fig. S2 EEM spectra of the soluble microbial products in water during the spore inacitivation in MNBs treatment group.

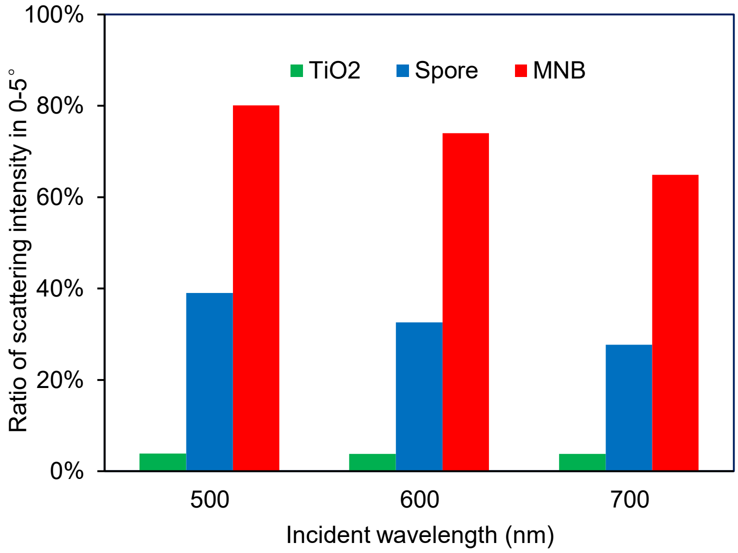

Fig. S3 The relative scattering intensity in the angle range *θ*=0-5° under different scenarios.

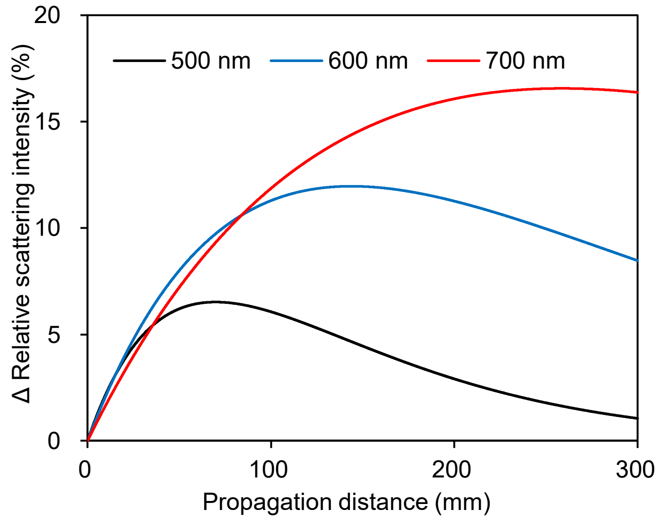

Fig. S4 The difference of relative scattering intensity at different propagation distances w/ and w/o MNBs at three incident wavelengths (500, 600, and 700 nm).

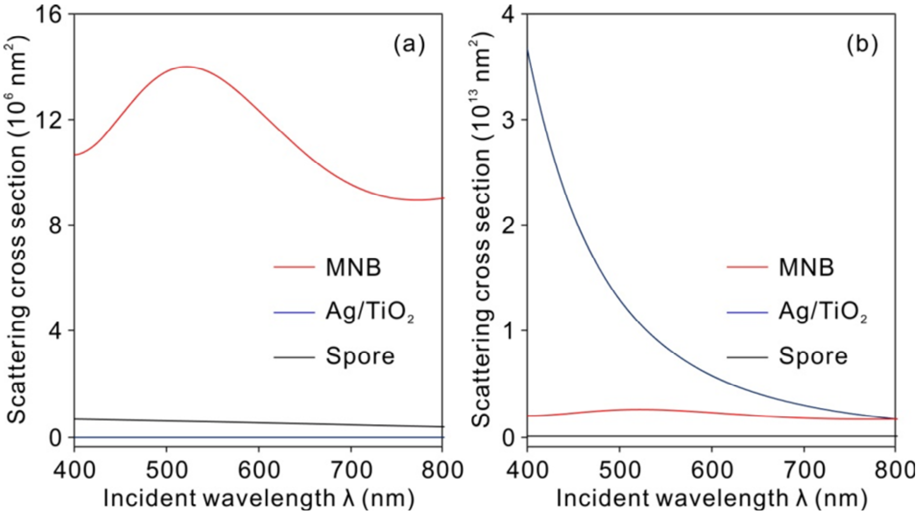

Fig. S5 Scattering cross section of single particle (a) and the total scattering cross section of all particles in suspension (b).

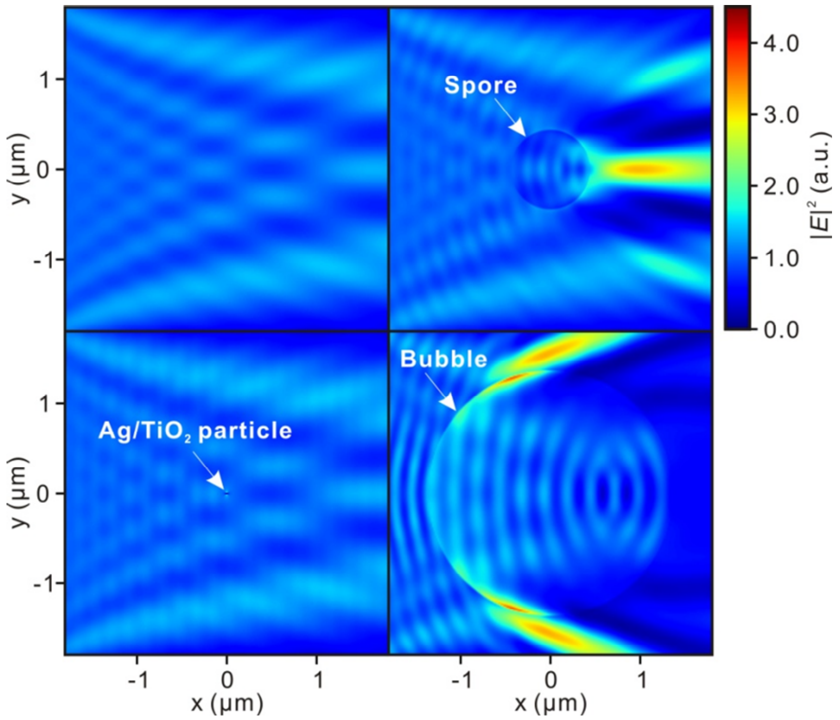

Fig. S6 FDTD simulation of the electric field distribution in target domain. The incident wavelength is 500 nm. (a) water alone; (b) near an illuminated spore; (c) near an illuminated Ag/TiO_2 particle; (d) near an illuminated MNB.

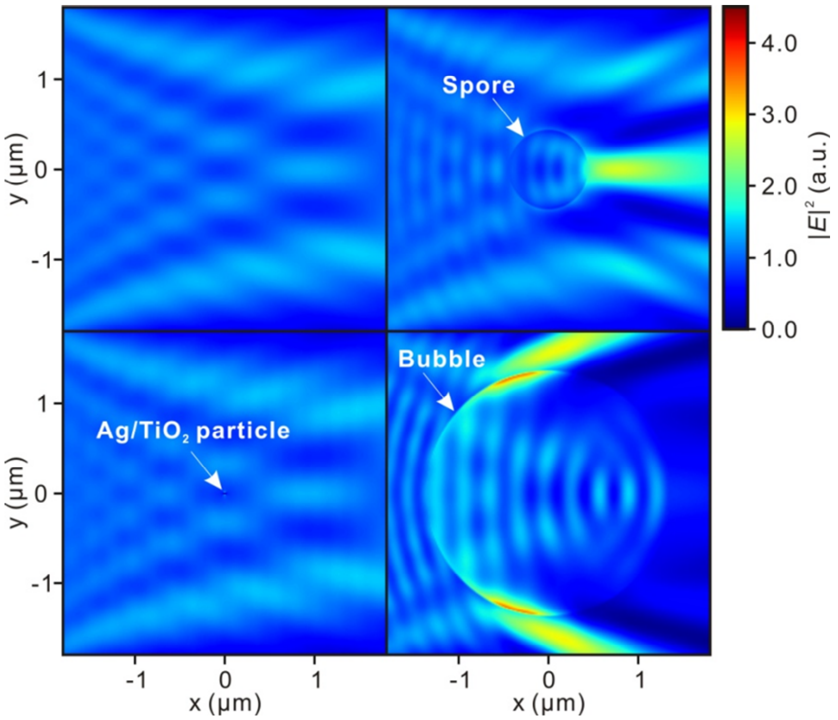

Fig. S7 FDTD simulation of the electric field distribution in target domain. The incident wavelength is 600 nm. (a) water alone; (b) near an illuminated spore; (c) near an illuminated Ag/TiO_2 particle; (d) near an illuminated MNB.

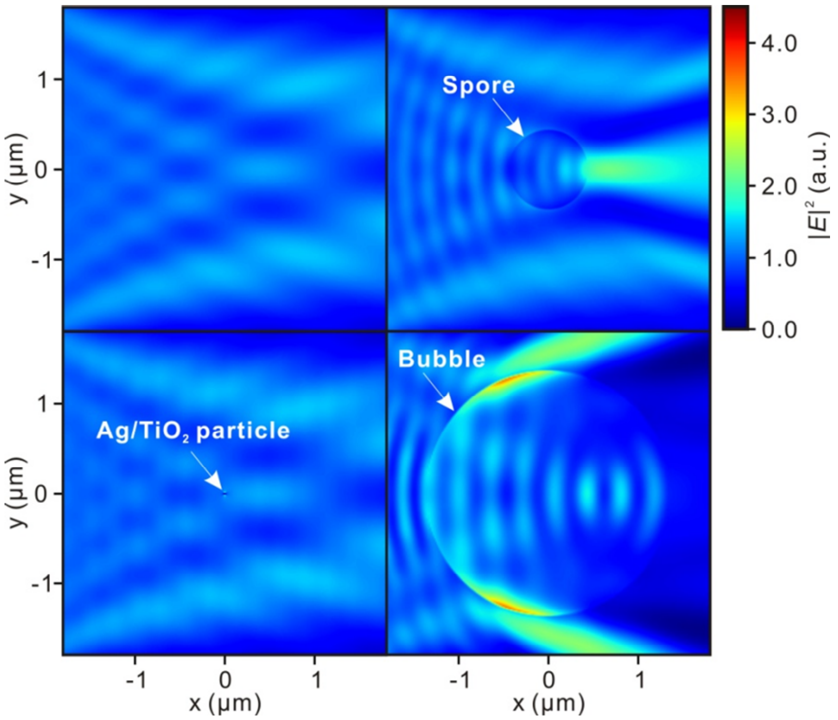

Fig. S8 FDTD simulation of the electric field distribution in target domain. The incident wavelength is 700 nm. (a) water alone; (b) near an illuminated spore; (c) near an illuminated Ag/TiO_2 particle; (d) near an illuminated MNB.

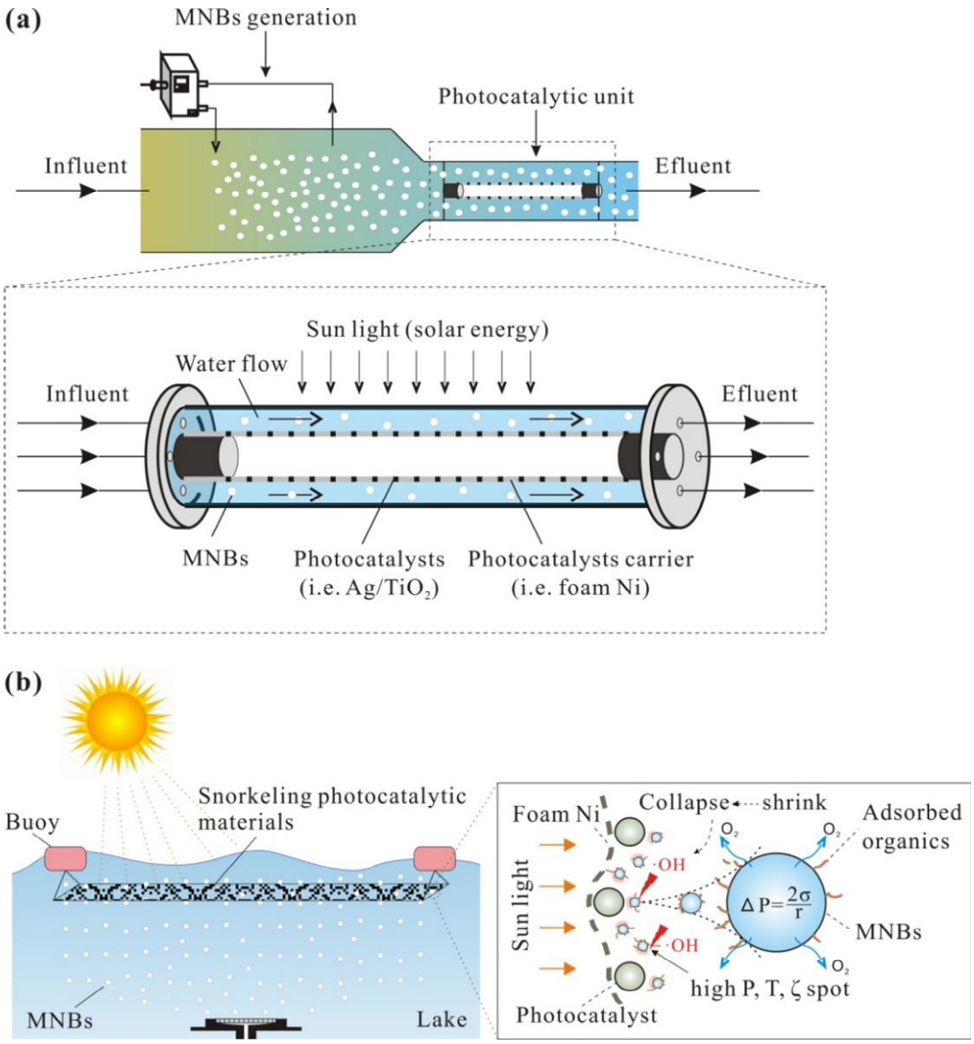

Fig. S9 Potential enhanced photocatalytic implementations in (a) fixed-bed reactor in advanced water and wastewater treatment plants, and (b) in combination with floating photocatalytic materials in open water.